inorganics

MDPI

Article

Synthesis of M-Doped $MoSe_2$ (M = Fe, Co, Ni) via Chemical Vapor Deposition for an Electrocatalytic Hydrogen Evolution Reaction

Xinya Chen [1], Xingchen Zhang [1], Jinying Zhang [2] and Zhiyong Wang [1,*]

[1] Key Laboratory of Advanced Light Conversion Materials and Biophotonics, School of Chemistry and Life Resources, Renmin University of China, Beijing 100872, China
[2] State Key Laboratory of Electrical Insulation and Power Equipment, Center of Nanomaterials for Renewable Energy (CNRE), School of Electrical Engineering, Xi'an Jiaotong University, Xi'an 710049, China
* Correspondence: zhiyongwang@ruc.edu.cn

Abstract: Given the high cost and limited availability of noble-metal-based catalysts in acidic media water electrolysis, developing cost-effective and high-performance non-noble metal catalysts is crucial for realizing large-scale hydrogen production. In this study, Fe-, Co-, and Ni-doped $MoSe_2$ nanomaterials were synthesized via chemical vapor deposition, and their electrocatalytic performance for the hydrogen evolution reaction (HER) was systematically evaluated. Characterization techniques including X-ray diffraction, X-ray photoelectron spectroscopy, transmission electron microscopy, scanning electron microscopy, and Raman spectroscopy were used to confirm the incorporation of doping elements and investigate their effects on the crystal structure and morphology of $MoSe_2$. Electrochemical tests, including linear sweep voltammetry and cyclic voltammetry, revealed that the doping of Fe, Co, and Ni significantly enhanced the HER catalytic activity of $MoSe_2$, with the Co-doped sample exhibiting the best performance, showing an overpotential of 0.293 V at 100 mA/cm^{-2} and a Tafel slope of 47 mV/dec. Furthermore, density functional theory calculations were employed to analyze the adsorption energy of hydrogen atoms on the catalysts, providing deeper insights into the role of doping in tuning the catalytic activity of $MoSe_2$. This study offers new theoretical support and experimental evidence for the application of transition metal-doped $MoSe_2$ in electrocatalysis.

Keywords: $MoSe_2$; chemical vapor deposition; doping; electrocatalysis; hydrogen evolution reaction

check for updates

Academic Editors: Axel Klein and Francis Verpoort

Received: 1 April 2025
Revised: 30 April 2025
Accepted: 6 May 2025
Published: 8 May 2025

Citation: Chen, X.; Zhang, X.; Zhang, J.; Wang, Z. Synthesis of M-Doped $MoSe_2$ (M = Fe, Co, Ni) via Chemical Vapor Deposition for an Electrocatalytic Hydrogen Evolution Reaction. *Inorganics* **2025**, *13*, 155. https://doi.org/10.3390/inorganics13050155

Copyright: © 2025 by the authors. Licensee MDPI, Basel, Switzerland. This article is an open access article distributed under the terms and conditions of the Creative Commons Attribution (CC BY) license (https://creativecommons.org/licenses/by/4.0/).

1. Introduction

With the rapid advancement of renewable energy technologies, water electrolysis has garnered considerable attention as a clean and sustainable approach to hydrogen production [1–4]. In particular, acidic water splitting offers simplicity in operations and high efficiency, making it promising for large-scale hydrogen generation. Currently, noble metals (e.g., platinum) exhibit the best catalytic performance in acidic media, but their high cost and limited availability impede widespread application [5–7]. Therefore, the development of cost-effective, high-performance non-noble metal electrocatalysts is crucial to advancing hydrogen energy technologies.

In this context, two-dimensional transition metal dichalcogenides (TMDs) have emerged as a major focus of electrocatalytic research, owing to their tunable band gaps, abundant active sites, and distinctive layered structures [8–10]. Among them, molybdenum diselenide ($MoSe_2$) has demonstrated promising theoretical catalytic activity due

to its layered structure and moderate hydrogen adsorption free energy [11]. However, the low intrinsic electrical conductivity of $MoSe_2$ severely limits its practical applications in electrocatalysis.

Recent advances demonstrate that transition metal doping can effectively tailor TMD's electronic configuration through synergistic lattice strain and charge redistribution effects [12–23]. For instance, theoretical studies by Chen et al. have predicted that Fe doping enhances $MoSe_2$'s metallic character by shifting the d-band center, while cobalt incorporation has been shown to optimize hydrogen adsorption kinetics on selenium vacancies [19]. Liu et al. computationally confirmed that Co doping optimizes the hydrogen adsorption energy ($\Delta G_{H^*} \approx 0.08$ eV) of $MoSe_2$ [20]. Currently, there is a lack of experimental studies systematically comparing catalytic performance among different doped $MoSe_2$ materials.

This study aims to synthesize Fe-, Co-, and Ni-doped $MoSe_2$ using the chemical vapor deposition (CVD) method and systematically compare their electrocatalytic performance in a hydrogen evolution reaction (HER) through a combination of experimental characterization and theoretical calculations. Their structure and electronic properties were studied using techniques such as X-ray diffraction (XRD), X-ray photoelectron spectroscopy (XPS), transmission electron microscopy (TEM), and Raman spectroscopy. In addition, density functional theory calculations are used to gain insight into the effects of doping on the hydrogen adsorption behavior and catalytic reaction pathways. This study not only elucidates the mechanism of transition metal doping to improve the catalytic performance of $MoSe_2$, but also provides important theoretical and experimental guidance for the design and optimization of novel HER electrocatalysts.

2. Results and Discussion

2.1. Morphology and Structure Analysis

Scanning electron microscopy (SEM) was used to systematically characterize the surface morphology of $MoSe_2$ and its Fe-, Co-, and Ni-doped variants. As shown in Figure 1a, undoped $MoSe_2$ exhibits a petal-like lamellar structure with interlaced layers, creating numerous edges and pores. In Figure 1b, Fe-doped $MoSe_2$ reveals a denser lamellar arrangement, accompanied by additional nanometer-scale protrusions and defects. Compared to the Fe-doped sample, Co-doped $MoSe_2$ (Figure 1c) displays larger grain sizes and a granular appearance, whereas Ni-doped $MoSe_2$ (Figure 1d) exhibits a similar granular structure to the Co-doped sample, but with smoother surfaces and a more uniform particle distribution. These findings suggest that introducing Fe, Co, or Ni significantly impacts the original petal-like layers of $MoSe_2$, producing denser and more regular lamellar or granular features. The film thicknesses of the pristine and doped $MoSe_2$ sample are about 1–2 μm.

Figure 2 provides a detailed analysis of the microstructure of $MoSe_2$ and its doped variants using high-resolution TEM (HRTEM), Selected area electron diffraction (SAED), and STEM-HAADF. Figure 2a,b show the HRTEM images of undoped $MoSe_2$, displaying clear lattice fringes with a lattice spacing of approximately 0.28 nm, corresponding to the (100) plane of $MoSe_2$. The Fast Fourier Transform (FFT) images within the red box further confirm the single-crystal nature of $MoSe_2$. Figure 2c presents the SAED pattern of $MoSe_2$, displaying a set of hexagonally arranged diffraction spots, indicating the presence of a well-ordered single-crystal structure. Figure 2d shows the STEM-HAADF image and its elemental distribution map of $MoSe_2$, demonstrating that Mo and Se are evenly distributed throughout the sample, confirming the uniformity of the $MoSe_2$ structure.

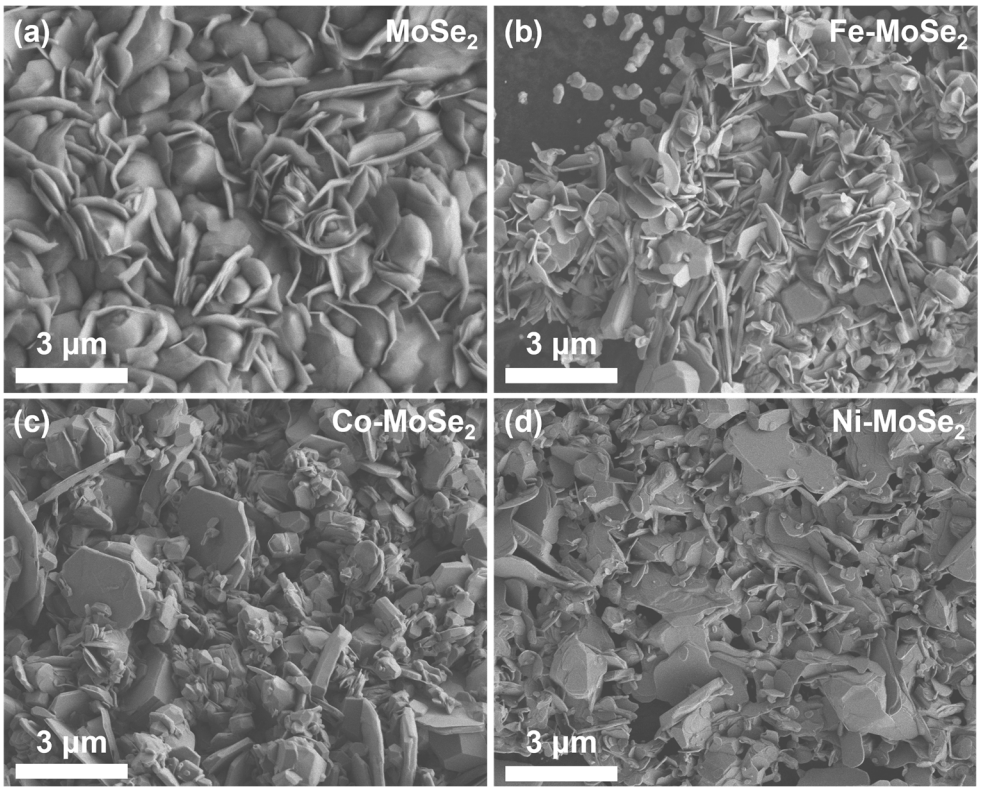


Figure 1. SEM images of (**a**) $MoSe_2$, (**b**) Fe-$MoSe_2$, (**c**) Co-$MoSe_2$, and (**d**) Ni-$MoSe_2$.

Figure 2e,f depict the HRTEM images of Fe-doped $MoSe_2$, with lattice spacings of 0.28 nm (corresponding to the $MoSe_2$ (100) plane) and 0.26 nm (corresponding to the $MoSe_2$ (102) plane). Figure 2g shows the corresponding SAED pattern, with diffraction spots arranged in a hexagonal pattern, confirming that the sample retains its single-crystal characteristics. Figure 2h presents the STEM-HAADF image and elemental distribution map of Fe-doped $MoSe_2$, where Fe is uniformly distributed within $MoSe_2$ without observable aggregation, suggesting that Fe has been successfully incorporated into $MoSe_2$ and may introduce additional defects and active sites, which could enhance its electrocatalytic performance.

Figure 2i,j show the HRTEM images of Co-doped $MoSe_2$, with lattice fringe spacings similar to those of the Fe-doped samples. The FFT images indicate that the single-crystal structure of $MoSe_2$ remains intact after Co incorporation. Figure 2k shows the SAED pattern of Co-doped $MoSe_2$, suggesting that Co doping does not significantly alter the single-crystal structure of $MoSe_2$. Figure 2l shows the STEM-HAADF image and elemental distribution map of Co-doped $MoSe_2$, where Co is evenly distributed, which may further increase the number of catalytic active sites, thereby enhancing the electrocatalytic performance.

Figure 2m,n depict the HRTEM images of Ni-doped $MoSe_2$, exhibiting lattice fringes similar to those of the Fe and Co-doped samples, indicating that the crystal structure of $MoSe_2$ remains largely unchanged after Ni doping. The FFT image is basically unchanged. Figure 2o shows the SAED pattern of Ni-doped $MoSe_2$, with regular diffraction spots, further confirming that the single-crystal structure of $MoSe_2$ is preserved after Ni doping. Figure 2p presents the STEM-HAADF image and elemental distribution map of Ni-doped $MoSe_2$, where Ni is uniformly distributed, providing additional active sites that may enhance its electrocatalytic performance.

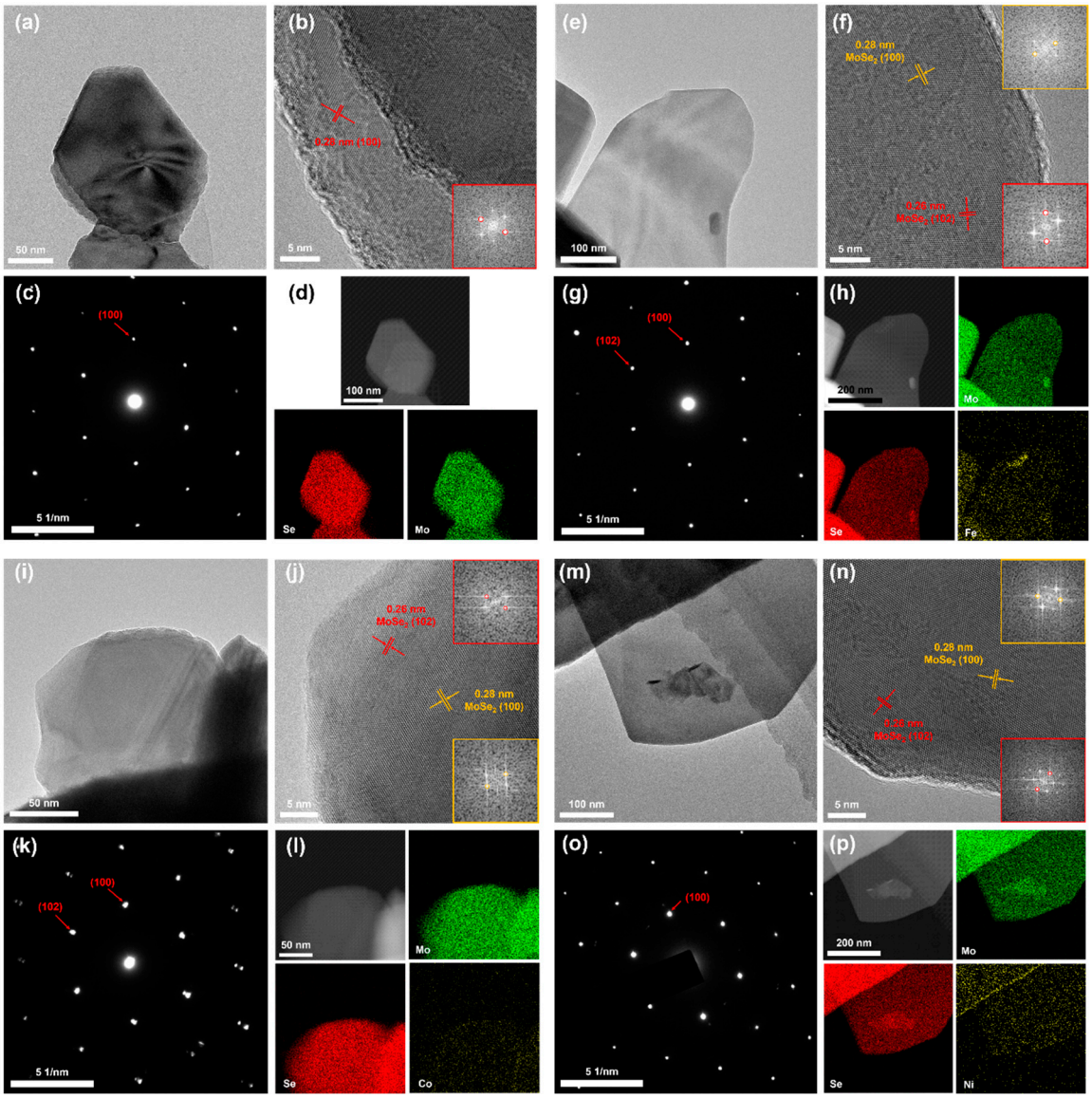


Figure 2. (**a**,**b**) HRTEM images of $MoSe_2$, with the corresponding FFT in the red box. (**c**) SAED pattern of $MoSe_2$. (**d**) STEM-HAADF image and EDS elemental mapping of Mo and Se. (**e**,**f**) HRTEM images of Fe-$MoSe_2$, with the insets showing the corresponding FFT patterns. (**g**) SAED pattern of Fe-$MoSe_2$. (**h**) STEM-HAADF image and EDS elemental mapping of Mo, Se, and Fe. (**i**,**j**) HRTEM images of Co-$MoSe_2$, with the insets showing the corresponding FFT patterns. (**k**) SAED pattern of Co-$MoSe_2$. (**l**) STEM-HAADF image and EDS elemental mapping of Mo, Se, and Co. (**m**,**n**) HRTEM images of Ni-$MoSe_2$, with the insets showing the corresponding FFT patterns. (**o**) SAED pattern of Ni-$MoSe_2$. (**p**) STEM-HAADF image and EDS elemental mapping of Mo, Se, and Ni.

2.2. Component Analysis

XPS analysis was conducted for Fe-doped $MoSe_2$. As shown in Figure 3a, the XPS analysis of Fe reveals that the Fe 2p spectrum exhibits remarkable splitting characteristics. The Fe $2p_{3/2}$ peak presents two main peaks at approximately 710.5 eV and 713.2 eV. The peaks are at approximately 723.9 eV and 727.0 eV in the Fe $2p_{1/2}$ spectrum. The XPS spectrum of Fe $2p_{3/2}$ and Fe $2p_{1/2}$ at 710.5 eV and 723.9 eV correspond to the Fe^{2+} state, and the XPS spectrum of Fe $2p_{3/2}$ and Fe $2p_{1/2}$ at 713.2 eV and 727.0 eV correspond to the Fe^{3+} state. Moreover, the shake-up satellite peaks near approximately 718 eV and 733 eV, typical features of Fe^{3+}, further confirm the presence of Fe^{3+} in the sample. Collectively, Fe in the sample primarily appears in the Fe^{2+} state, with a lesser fraction of Fe^{3+}, resulting in

a mixed valence environment. This valence state distribution is attributed to the partial cleavage of Fe-Se bonds during the preparation process, leading to the oxidation of Fe atoms, which is highly likely to have a significant impact on the electrochemical and catalytic properties of the sample.

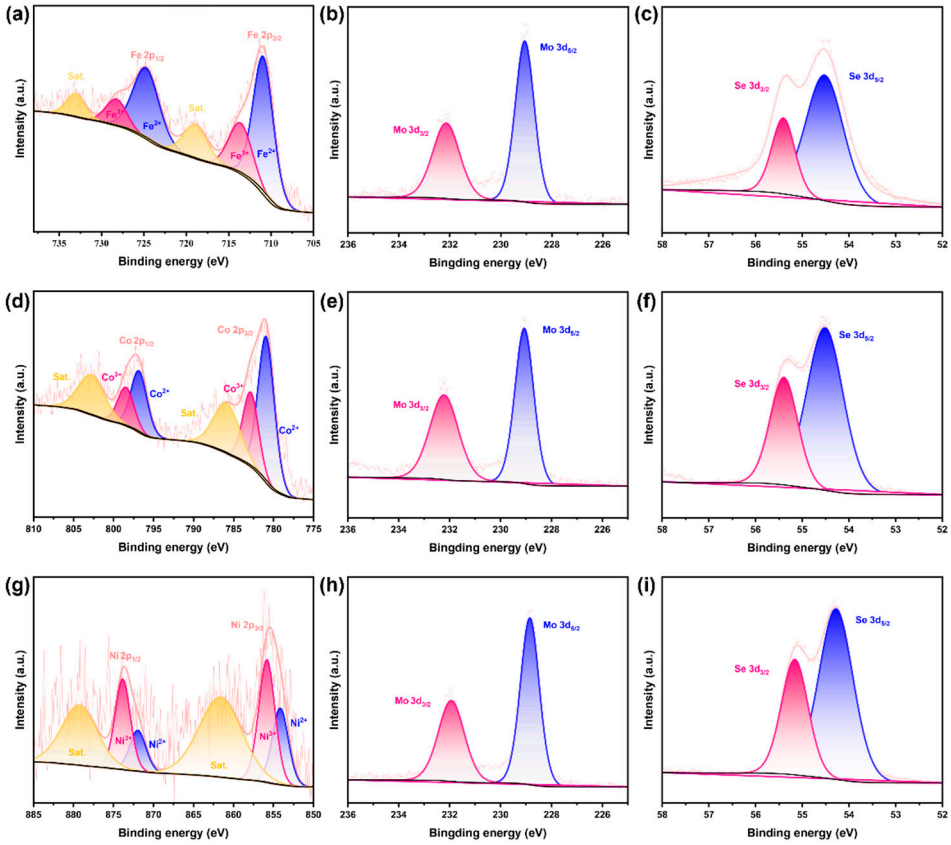


Figure 3. XPS spectra of Fe-$MoSe_2$ showing the signals of (**a**) Fe 2p, (**b**) Mo 3d, and (**c**) Se 3d. XPS spectra of Co-$MoSe_2$ showing the signals of (**d**) Co 2p, (**e**) Mo 3d, and (**f**) Se 3d. XPS spectra of Ni-$MoSe_2$ showing the signals of (**g**) Ni 2p, (**h**) Mo 3d, and (**i**) Se 3d.

As depicted in Figure 3d, analysis of the Co XPS spectrum shows that both the Co $2p_{3/2}$ and Co $2p_{1/2}$ peaks are split. The Co $2p_{3/2}$ peaks at approximately 781.0 eV and 782.7 eV, as well as the Co $2p_{1/2}$ peaks at approximately 797.0 eV and 798.5 eV, correspond to Co^{2+} and Co^{3+}, respectively. Meanwhile, the typical Co^{2+} shake-up satellite peaks near approximately 786.5 eV and 803.0 eV indicate that Co in the sample mainly exists in a mixed valence state of Co^{2+} and Co^{3+}, with Co^{2+} being dominant. This strongly demonstrates that Co has been successfully incorporated into the $MoSe_2$ lattice to form Co-Se bonds, a structure that plays a crucial role in maintaining material stability and regulating its electronic properties.

As shown in Figure 3g, regarding the XPS analysis of Ni, the splitting features of the Ni $2p_{3/2}$ and Ni $2p_{1/2}$ peaks indicate that the Ni $2p_{3/2}$ peaks at approximately 854.0 eV and 855.5 eV, along with the Ni $2p_{1/2}$ peaks at approximately 872.0 eV and 874.2 eV, correspond to Ni^{2+} and Ni^{3+}, respectively. The shake-up satellite peaks at 861.7 eV and 879.5 eV are consistent with the coordination environment of Ni^{2+}. The Ni in the sample mainly exists in a mixed valence state of Ni^{3+} and Ni^{2+}, and Ni^{3+} is the main one. This implies that the partial oxidation of Ni occurred during the preparation process, accompanied by changes in the Ni-Se structure, which may significantly influence the electrochemical and catalytic properties of the sample.

Notably, as illustrated in Figure 3b,e,h for Mo 3d and Figure 3c,f,i for Se 3d, the XPS spectra of Mo 3d and Se 3d show that, regardless of Fe, Co, or Ni doping, the Mo $3d_{5/2}$ peak remains at 229.5 eV, the Mo $3d_{3/2}$ peak at 232.5 eV, and the Se $3d_{5/2}$ and Se $3d_{3/2}$ peaks at 54.5 eV and 55.5 eV, respectively. This clearly indicates that the doping process has a minimal effect on the chemical states of Mo and Se, and that the Mo-Se skeleton structure of $MoSe_2$ remains highly stable. Additionally, quantitative analysis results show that the contents of Fe, Co, and Ni are 9.01%, 5.44%, and 2.24%, respectively, further confirming the successful implementation of the doping process.

2.3. Optical and Crystal Structure Analysis

Additionally, the Raman scattering spectra and XRD patterns of both doped and undoped $MoSe_2$ provide insights into the effects of doping on the material's structure and vibrational modes.

Figure 4a shows the Raman spectra of Fe/Co/Ni-$MoSe_2$ and $MoSe_2$. Undoped $MoSe_2$ exhibits two main Raman active peaks at approximately 238 cm^{-1} (E_{2g}) and 285 cm^{-1} (A_{1g}), corresponding to the interlayer vibrational mode (E_{2g}) and the in-plane vibrational mode (A_{1g}) of $MoSe_2$. These peaks indicate the well-defined layered structure of $MoSe_2$. For the Fe-, Co-, and Ni-doped $MoSe_2$ samples, the shapes and positions of the E_{2g} and A_{1g} peaks undergo slight shifts towards lower frequencies, suggesting that doping has caused minor changes in the lattice. Particularly, Co-doped $MoSe_2$ shows a slight splitting of the E_{2g} peak, possibly due to lattice stress and distortion after Co incorporation. This splitting may result from local lattice deformation or dislocation introduced by Co, leading to subtle changes in the vibrational modes. Fe- and Ni-doped samples show similar peak shifts, but no obvious splitting like the Co-doped sample, indicating that Fe and Ni doping have a relatively smaller effect on the lattice.

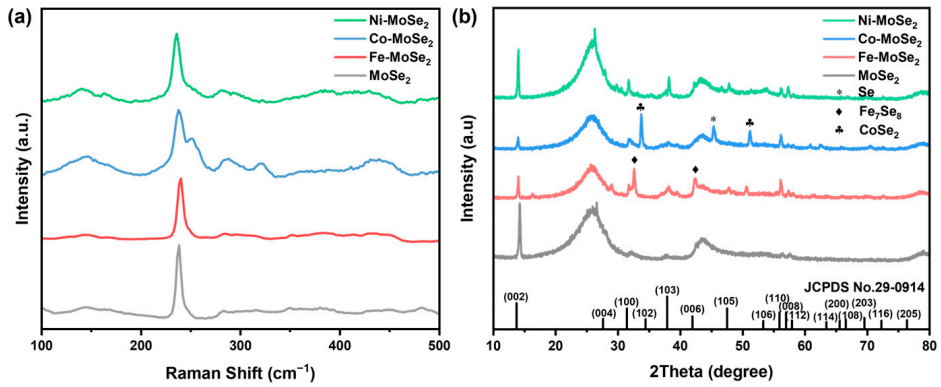


Figure 4. (**a**) Raman scattering spectra and (**b**) XRD patterns of Fe/Co/Ni-$MoSe_2$ and $MoSe_2$.

The crystal structures of pristine and M-doped $MoSe_2$ were investigated using XRD, as shown in Figure 4b. All samples exhibit dominant diffraction peaks corresponding to the hexagonal 2H-$MoSe_2$ phase (JCPDS No.29-0914), including the characteristic (002) peak at ~13.7° (interlayer stacking), (100) peak at ~31.4°, and (110) peak at ~55.9°, confirming the retention of the layered structure after doping.

The sharp (002) peak with a full width at half maximum (FWHM) of ~0.3° correlates with the vertically aligned nanosheet morphology observed in SEM (Figure 1a–d). For the Fe-doped sample, the peaks at 32.5° and 43.4° are assigned to Fe_7Se_8, while for the Co-doped sample, the peaks at 34.4° and 51.9° correspond to $CoSe_2$, and the peak at 45.7° is attributed to elemental Se. These results indicate that partial selenization of the metal dopants occurred during the reaction process. The broad peaks near 25° and 43° originate from the glassy carbon substrate, as verified by control experiments (Figure S1 of the Supplementary Materials).

2.4. Electrochemical Characterization

The electrocatalytic performance of $MoSe_2$, glassy carbon (GC), Pt/C, and Fe-/Co-/Ni-doped $MoSe_2$ catalysts was evaluated through polarization curves, Tafel slopes, and double-layer capacitance (C_{dl}) calculations. As shown in Figure 5a, in 0.5 M H_2SO_4 solution, the polarization curves clearly show the HER activity of each catalyst: When the current density reaches 100 mA/cm^2, Pt/C has the lowest overpotential (only requiring approximately −0.149 V), serving as a benchmark to exhibit excellent HER activity. Pure $MoSe_2$ requires approximately −0.5 V, while Fe-$MoSe_2$ (−0.367 V), Co-$MoSe_2$ (−0.293 V), and Ni-$MoSe_2$ (−0.401 V) show significantly reduced overpotentials compared with pure $MoSe_2$. Among them, Co-$MoSe_2$ has the most obvious reduction, indicating that doping elements effectively improve the electrocatalytic performance of $MoSe_2$. The GC electrode has extremely weak catalytic performance due to its high overpotential of −1.424 V (Figure S2 of the Supplementary Materials). The overpotential of the Co-$MoSe_2$ at 100 mA/cm^2 is smaller than that of the previously reported Ni-$MoSe_2$ catalyst [24]. Combined with the Tafel slopes in Figure 5b, Pt/C has the smallest slope (fastest charge transfer). Co-$MoSe_2$ has a Tafel slope of 47 mV/dec (close to Pt/C), Ni-$MoSe_2$ shows 110 mV/dec, and Fe-$MoSe_2$ shows 75 mV/dec—all lower than pure $MoSe_2$ (172 mV/dec), further indicating that doping optimizes the catalytic reaction kinetics. Additionally, to systematically explore the catalytic enhancement effects of Fe, Co, and Ni doping on $MoSe_2$, $FeSe_2$, $CoSe_2$, and $NiSe_2$ were synthesized in this study. Their electrocatalytic performance was evaluated via LSV. The results showed that the performance of these selenides was lower than that of pure $MoSe_2$, thus ruling out the interference of selenides themselves on the catalytic performance. More details can be found in Figure S3 of the Supplementary Materials.

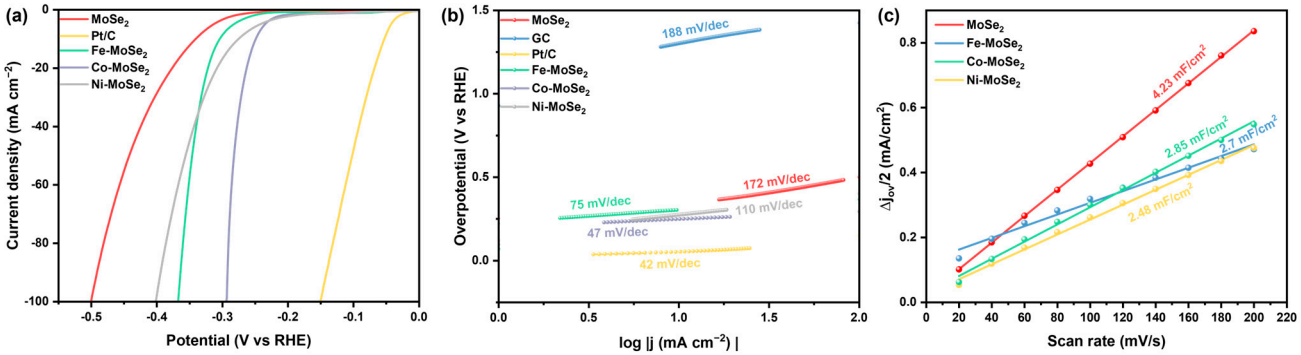


Figure 5. (**a**) Polarization curves of $MoSe_2$, Pt/C, and Fe/Co/Ni-$MoSe_2$ catalysts. (**b**) Calculated Tafel slopes. Testing was performed in 0.5 M H_2SO_4 with a scan rate of 50 mV/s. (**c**) C_{dl} of $MoSe_2$ and Fe/Co/Ni-$MoSe_2$.

To thoroughly assess the electrochemical catalytic performance of our electrocatalysts and enable meaningful comparison with previous studies, we have compiled the catalytic properties of various MoX_2-based catalysts in Table 1. Comparative analysis reveals that the Co-doped $MoSe_2$ catalyst in this work demonstrates superior electrocatalytic performance, as manifested by its reduced overpotential and lower Tafel slope relative to other catalysts. For example, the reported $Ni_{0.15}Mo_{0.85}Se_2$ catalyst requires an overpotential of 0.32 V to reach 90 mA/cm^2 [25], whereas our Co-doped $MoSe_2$ catalyst achieves a higher current density of 100 mA/cm^2 at a lower overpotential of 0.29 V. The Co-doped $MoSe_2$ catalyst also shows better performance than $MoSe_2$ decorated with Co and Ni nanoparticles [26] and Fe-, Co-, and Ni-doped MoS_2 [27]. While the Tafel slopes of Fe-, Co-, or Ni-doped MoS_2 typically range from 66 to 94 mV/dec, our Co-doped $MoSe_2$ exhibits a significantly lower Tafel slope of 47 mV/dec, indicating enhanced reaction kinetics. Compared with the

graphene/$MoSe_2$ composites reported previously [28], the Co-doped $MoSe_2$ catalyst also exhibits a lower Tafel slope (80 vs. 47 mV/dec).

Table 1. The electrochemical catalytic performance of MoX_2-based catalysts.

Electrocatalyst	Electrolyte	Current Density (mA cm^{-2})	Overpotential (mV)	Tafel Slope (mV dev^{-1})
Co-$MoSe_2$ (this work)	0.5 M H_2SO_4	100	293	47
Fe-$MoSe_2$ (this work)	0.5 M H_2SO_4	100	367	75
Ni-$MoSe_2$ (this work)	0.5 M H_2SO_4	100	401	110
Ni-$MoSe_2$ [24]	1.0 M KOH	50	455	96
$MoSe_2$/carbon cloth [29]	0.5 M H_2SO_4	21 60	250 300	76
$Ni_{0.15}Mo_{0.85}Se_2$ [25]	0.5 M H_2SO_4	10 90	180 ~320	67
$MoSe_2$@Co [26]	1 M KOH	10	391	109
$MoSe_2$@Ni [26]	1 M KOH	10	367	227
$MoSe_2$@CoNi [26]	1 M KOH	10	378	170
graphene/$MoSe_2$ [28]	0.5 M H_2SO_4	100	~210	80
Ni-MoS_2 [27]	0.5 M H_2SO_4	10 35	302 ~360	66
Co-MoS_2 [27]	0.5 M H_2SO_4	10 35	350 ~550	69
Fe-MoS_2 [27]	0.5 M H_2SO_4	10 35	490 ~700	94

Furthermore, this study analyzed the electrochemical active surface areas (ECSAs) of the catalysts. The ECSA was evaluated by C_{dl} using cyclic voltammetry (CV) at various scan rates in the potential range from 0 to 0.2 V versus RHE (Figure S4 of the Supplementary Materials). Typically, the ECSA is directly proportional to the C_{dl} of the electrode, expressed as ECSA = C_{dl}/C_s, where C_s represents the specific capacitance of the catalysts per unit area under identical electrolyte conditions. The specific capacitance typically falls within a reported range of 0.015–0.110 mF/cm^2 in acidic solutions. The general specific capacitance of 0.035 mF/cm^2 was used to estimate the ECSA in this work [30]. In Figure 5c, the ECSA values of Fe-/Co-/Ni-doped $MoSe_2$ are 77.14, 70.86, and 81.43 cm^2 respectively, slightly lower than that of pure $MoSe_2$ (120.9 cm^2). Consequently, while the ECSA is an important parameter for understanding electrocatalytic behavior, it may not be the predominant factor governing the enhanced HER performance of Fe-/Co-/Ni-doped $MoSe_2$.

2.5. Theoretical Calculation

To gain deeper insights into the active sites of Fe-, Co-, and Ni-doped $MoSe_2$ (M-$MoSe_2$) in the HER, we performed density functional theory (DFT) calculations on Fe-$MoSe_2$, Co-$MoSe_2$, Ni-$MoSe_2$, and pristine $MoSe_2$. The catalytic activity was evaluated using the ΔG_H, which reflects the hydrogen adsorption capability on the material surface. An effective HER catalyst typically exhibits a ΔG_H value close to zero, indicating moderate hydrogen adsorption strength that facilitates efficient HER. A ΔG_H that is too positive (weak adsorption) or too negative (strong adsorption) would hinder the reaction. Thus, the ideal HER catalyst should have $\Delta G_H \approx 0$ eV.

In this study, we analyzed multiple potential hydrogen adsorption sites on M-$MoSe_2$, including basal plane Se sites (plane Se), metallic edge Mo sites (edge Mo), and non-metallic edge M/Se sites (edge M/edge Se). For comparison, we also calculated hydrogen adsorption on pristine $MoSe_2$ at basal plane Se sites (plane Se), metallic edge Mo sites (edge Mo), and non-metallic edge Se sites (edge Se). The optimized structure is shown in Figure 6, and the calculated ΔG value is shown in Figure 7.

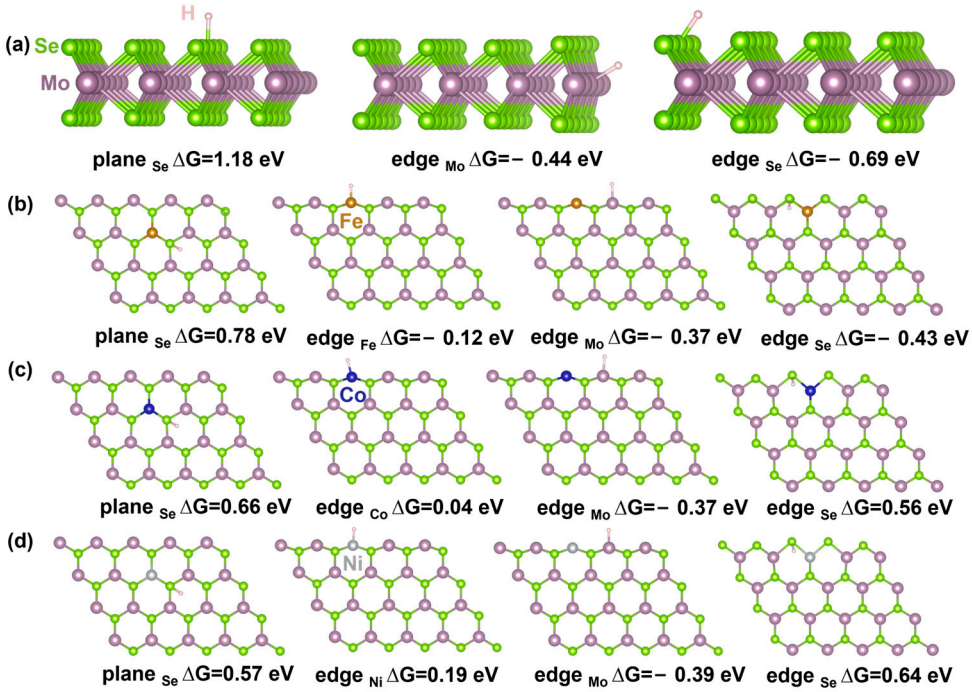


Figure 6. DFT-optimized structures showing H atom adsorption on different positions of (**a**) $MoSe_2$, (**b**) Fe-$MoSe_2$, (**c**) Co-$MoSe_2$, and (**d**) Ni-$MoSe_2$.

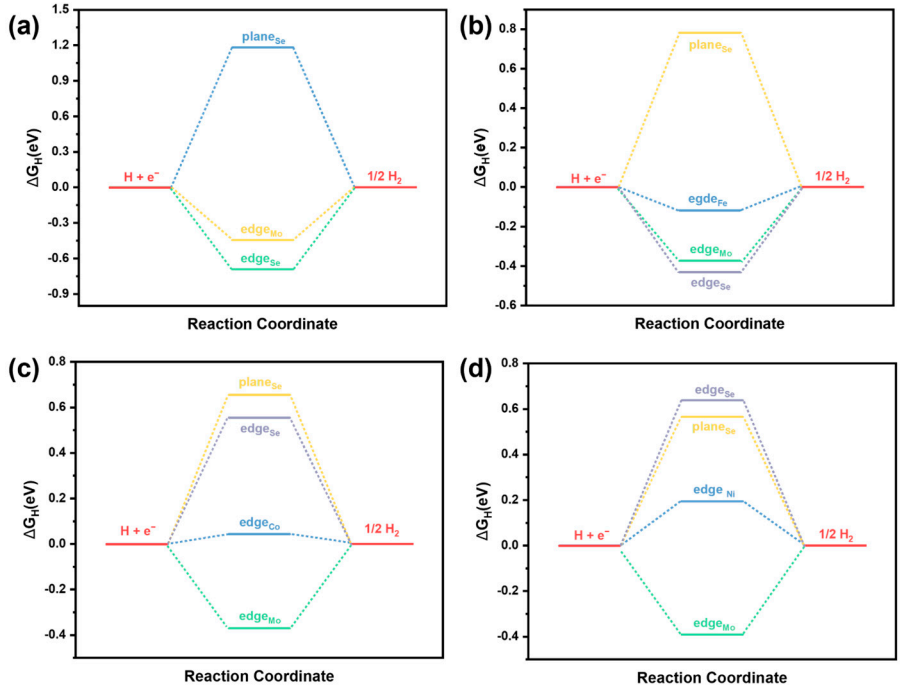


Figure 7. The calculated ΔG for H atom adsorption on different positions of (**a**) $MoSe_2$, (**b**) Fe-$MoSe_2$, (**c**) Co-$MoSe_2$, and (**d**) Ni-$MoSe_2$.

For pristine MoSe2, the ΔG values for hydrogen adsorption at basal plane Se sites, metallic edge Mo sites, and non-metallic edge Se sites are 1.18, −0.44, and −0.69 eV, respectively. Upon Fe doping, the ΔG value at basal plane Se sites decreases to 0.78 eV, while the metallic edge Mo sites show a ΔG of −0.37 eV; notably, the edge Fe site exhibits a significantly lower ΔG of −0.12 eV, and the adjacent edge Se site is −0.43 eV. With Co doping, the ΔG at basal plane Se sites is further reduced to 0.66 eV, the metallic edge Mo site remains at −0.37 eV, and the edge Co site approaches a near-ideal ΔG of 0.04 eV, with adjacent edge Se sites at 0.56 eV. In the Ni-doped sample, the ΔG values are 0.57 eV (basal plane Se), −0.39 eV (metallic edge Mo), and 0.19 eV (edge Ni), while the adjacent edge Se sites near Ni exhibit a ΔG of 0.64 eV. Overall, these findings suggest that doping MoSe2 with transition metals can optimize hydrogen adsorption and thus improve its electrocatalytic performance.

3. Experimental

3.1. Sample Preparation

Fe-, Co-, and Ni-doped $MoSe_2$ were synthesized using the chemical vapor deposition method (Figure 8a). Initially, a 1 cm × 1 cm GC was sonicated in distilled water and ethanol for 10 min each to remove surface impurities. The precursor solution was prepared as follows: $(NH_4)_6Mo_7O_{24}{\cdot}4H_2O$ was dissolved in 1 mL of water to obtain a 0.0121 mol/L solution, which contained approximately 8.16 mg Mo per mL. For doping purposes, $FeCl_2$ (0.146 mol/L, ~8.16 mg Fe/mL), $CoCl_2{\cdot}6H_2O$ (0.139 mol/L, ~8.16 mg Co/mL), and $NiCl_2$ (0.139 mol/L, ~8.16 mg Ni/mL) were each dissolved in 1 mL of deionized water. Approximately 4–5 drops (equivalent to ~0.200–0.250 mL) of the precursor solution were uniformly drop-cast onto the surface of a pre-cleaned 1 cm × 1 cm GC, forming a full surface coverage. The sample was then dried at 60 °C for 1 h.

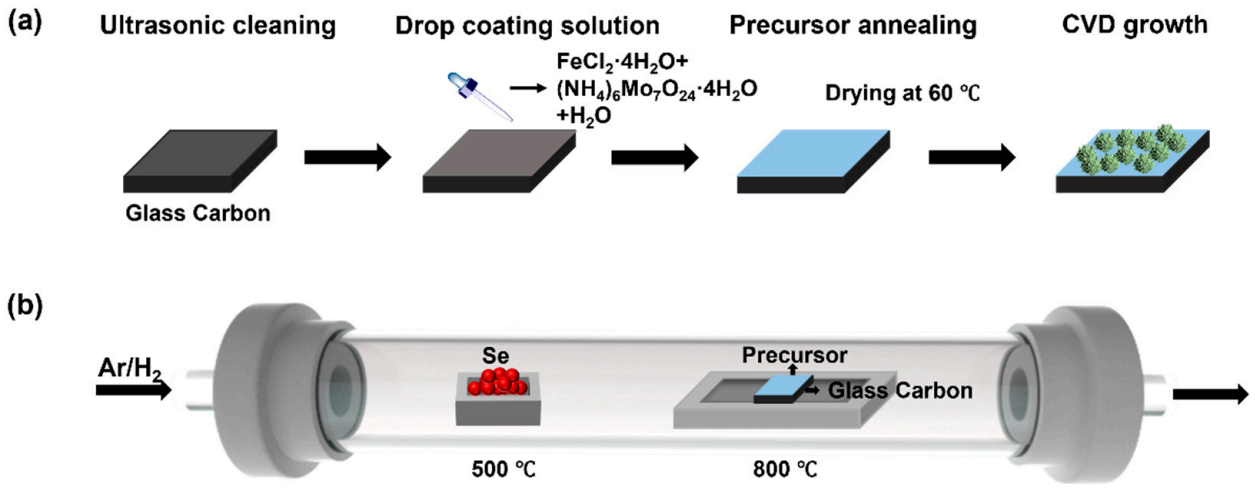


Figure 8. (**a**) Schematic diagram of the preparation process for Fe-doped $MoSe_2$. (**b**) Schematic diagram of the CVD system used to synthesize transition metal-doped $MoSe_2$ nanosheets.

The dried GC substrate was placed on the right side of a tube furnace, with 75 mg of Se powder placed in a porcelain boat on the left side as the Se source (Figure 8b). During the experiment, the temperatures on both sides were raised simultaneously, with the left side reaching 500 °C and the right side reaching 800 °C over a 40 min heating period. Ar gas was introduced at a flow rate of 100 sccm. Once the target temperatures were reached, the samples were kept at these temperatures for 15 min, while the atmosphere was adjusted to a 100 sccm Ar/H_2 gas mixture (9:1). Afterward, the heating system was turned off, and the samples were allowed to cool naturally to room temperature, yielding Fe-, Co-, and

Ni-doped $MoSe_2$ nanomaterials. To evaluate the impact of doping on the electrocatalytic performance of $MoSe_2$, undoped $MoSe_2$ was synthesized under the same conditions and compared with the doped samples.

3.2. Characterization Methods

Various techniques were employed to systematically analyze the materials. A Hitachi SU-8010 scanning electron microscope (manufactured by Hitachi High-Tech Corporation, Tokyo, Japan) was used to examine the surface morphology, while a JEOL F200 transmission electron microscope (200 kV, equipped with an Oxford X-MaxN 80T IE250 EDS; manufactured by JEOL Ltd., Tokyo, Japan) utilized DigitalMicrograph 3.5 software for image processing and data analysis, providing insights into the microstructure and lattice fringes. The crystal structure was assessed via X-ray diffraction using Cu Kα radiation (λ = 1.5406 Å) with a Shimadzu XRD-7000 X-ray diffractometer (manufactured by Shimadzu Corporation, Kyoto, Japan), and the data was processed with Origin 2022 software. The Raman spectra were acquired on a Horiba Xplora spectrometer (manufactured by Horiba Scientific, Kyoto, Japan) with a 532 nm laser source, and the spectral data was analyzed using LabSpec 6.3 software. Furthermore, X-ray photoelectron spectroscopy was performed on a Thermo Scientific K-Alpha instrument (manufactured by Thermo Fisher Scientific Inc., Waltham, MA, USA), and the elemental composition and chemical states of the samples were determined through Avantage 5.9 software.

3.3. Electrochemical Measurements

Electrochemical tests were performed using a CHI660E electrochemical work station (manufactured by Shanghai Chenhua Instrument Co., Ltd., Shanghai, China). GC electrodes loaded with Fe-, Co-, and Ni-doped $MoSe_2$ catalysts were used as the working electrodes, with Ag/AgCl and Pt electrodes serving as the reference and counter electrodes, respectively. All potentials were referenced to the reversible hydrogen electrode (RHE), calculated using the following formula: E_{RHE} = E(Ag/AgCl) + 0.059 pH + 0.197 V. LSV was carried out in a 0.5 M H_2SO_4 solution at a scan rate of 50 mV/s, with a 95% ohmic drop (IR) correction applied to all results. The Tafel slope, derived from the LSV curves, was used to evaluate the electrocatalytic reaction kinetics. Additionally, CV was performed in the potential range of 0–0.2 V vs. RHE at various scan rates (20–200 mV/s) to determine the double-layer capacitance.

3.4. Computational Details

First-principle calculations based on DFT were performed using the Vienna Ab initio Simulation Package (VASP) [31–33]. The exchange–correlation interactions were described by the Perdew–Burke–Ernzerhof (PBE) [34] functional within the generalized gradient approximation (GGA). For structural optimization, the energy change, maximum force, and maximum displacement convergence criteria were set to 2.0×10^{-5} Ha, 0.004 Ha $Å^{-1}$, and 0.005 Å, respectively. A $3 \times 3 \times 1$ k-point grid based on the Monkhorst–Pack scheme was used for Brillouin zone integration. The plane wave cutoff energy in VASP was set to 400 eV, and spin polarization effects were included in all calculations. Structural optimizations continued until the residual forces on each atom were reduced to less than 0.01 eV/Å.

To evaluate the catalytic activity of Fe-/Co-/Ni-doped $MoSe_2$ for the HER, we calculated the hydrogen adsorption energy (ΔE_H) at different active sites, defined as follows:

$$\Delta E_H = E_A - E_P - 0.5E_{H_2}$$

where E_A represents the energy of the catalyst with a single hydrogen atom adsorbed, E_P is the energy of the pristine catalyst, and E_{H_2} is the energy of a hydrogen molecule in the gas phase.

To further assess the hydrogen adsorption thermodynamics, we incorporated zero-point energy (ΔE_{ZPE}) and entropy (ΔS) corrections to determine the Gibbs free energy of hydrogen adsorption (ΔG_H), calculated as follows:

$$\Delta G_H = \Delta E_H + \Delta E_{ZPE} - T\Delta S$$

where T is the temperature (set to 298.15 K). These calculations provide insights into how Fe, Co, and Ni doping influence the hydrogen adsorption properties of $MoSe_2$, potentially enhancing its catalytic performance for HER.

4. Conclusions

We successfully synthesized Fe-, Co-, and Ni-doped $MoSe_2$ via CVD and systematically investigated their morphology, structure, and electrocatalytic performance. The results demonstrate that doping elements not only significantly altered the morphology of $MoSe_2$, but also enhanced its HER performance by introducing defects and optimizing the electronic structure. DFT calculations further confirmed that metal doping effectively reduces ΔG at active sites and enhances catalytic activity. Among the doped samples, Co-doped $MoSe_2$ exhibited the best catalytic activity, with an onset overpotential of 0.293 mV at 100 mA/cm^{-2} and a Tafel slope of 47 mV/dec. This study provides new insights into the application of transition metal-doped $MoSe_2$ in electrocatalysis.

Supplementary Materials: The following supporting information can be downloaded at: https://www.mdpi.com/article/10.3390/inorganics13050155/s1. Figure S1: XRD patterns of GC, Fe/Co/Ni-$MoSe_2$, and $MoSe_2$. Figure S2: Polarization curves of $MoSe_2$, GC, Pt/C, and Fe/Co/Ni-$MoSe_2$ catalysts. Figure S3: Polarization curves of (a) $MoSe_2$, Fe-$MoSe_2$, and $FeSe_2$ catalysts, (b) $MoSe_2$, Co-$MoSe_2$, and $CoSe_2$ catalysts, (c) $MoSe_2$, Ni-$MoSe_2$, and $NiSe_2$ catalysts. Figure S4: CV curves of $MoSe_2$ (a), Fe-$MoSe_2$ (b), Co-$MoSe_2$ (c), and Ni-$MoSe_2$ (d) at various scan rates (20 mV s^{-1}, 40 mV s^{-1}, 60 mV s^{-1}, 80 mV s^{-1}, 100 mV s^{-1}, 120 mV s^{-1}, 140 mV s^{-1}, 160 mV s^{-1}, 180 mV s^{-1}, 200 mV s^{-1}) in the potential range of 0~0.2 (vs. RHE).

Author Contributions: X.C.: investigation, data curation, formal analysis, writing—original draft preparation. X.Z.: data curation, software, formal analysis. J.Z.: methodology, data curation, resources. Z.W.: conceptualization, methodology, validation, writing—review and editing, visualization, supervision, project administration. All authors have read and agreed to the published version of the manuscript.

Funding: This research received no external funding.

Data Availability Statement: The original contributions presented in this study are included in the article and Supplementary Materials. Further inquiries can be directed to the corresponding author.

Acknowledgments: Resources supporting this work were provided by the Public Computing Cloud Platform of Renmin University of China. The authors thank the Office of Research Infrastructure of Renmin University of China for the laboratory facilities and technical support in sample characterization.

Conflicts of Interest: There are no conflicts of interest to declare.

References

1. Qiao, D.; Yun, S.; Sun, M.L.; Dang, J.E.; Zhang, Y.W.; Yuan, S.X.; Yang, G.P.; Yang, T.X.; Gao, Z.; Wang, Z.G. 1D/3D Trepang-Like N-Modified Carbon Confined Bimetal Carbides and Metal Cobalt: Boosting Electron Transfer via Dual Mott-Schottky Heterojunctions Triggered Built-In Electric Fields for Efficient Hydrogen Evolution and Tri-Iodide Reduction. *Appl. Catal. B Environ.* **2023**, *334*, 122830. [CrossRef]
2. Wang, L.Q.; Hao, Y.X.; Deng, L.M.; Hu, F.; Zhao, S.; Li, L.L.; Peng, S.J. Rapid Complete Reconfiguration Induced Actual Active Species for Industrial Hydrogen Evolution Reaction. *Nat. Commun.* **2022**, *13*, 5785. [CrossRef]
3. Sarwar, S.; Ali, A.; Wang, Y.F.; Ahasan, M.R.; Wang, R.G.; Adamczyk, A.J.; Zhang, X.Y. Enhancement of Hydrogen Evolution Reaction Activity Using Metal–Rich Molybdenum Sulfotelluride with Graphene Support: A Combined Experimental and Computational Study. *Nano Energy* **2021**, *90*, 106599. [CrossRef]
4. Zhang, Z.Y.; Tian, H.; Bian, L.; Liu, S.Z.; Liu, Y.; Wang, Z.L. Cu-Zn-Based Alloy/Oxide Interfaces for Enhanced Electroreduction of CO_2 to C_2^+ Products. *J. Energy Chem.* **2023**, *83*, 90–97. [CrossRef]
5. Wan, C.Z.; Zhang, Z.S.; Dong, J.C.; Xu, M.J.; Pu, H.T.; Baumann, D.; Lin, Z.Y.; Wang, S.B.; Huang, J.; Shah, A.H.; et al. Amorphous Nickel Hydroxide Shell Tailors Local Chemical Environment on Platinum Surface for Alkaline Hydrogen Evolution Reaction. *Nat. Mater.* **2023**, *22*, 1022–1029. [CrossRef]
6. Zhang, J.S.; Zhang, X.L.; Shi, C.; Xia, G.Q.; Li, H.; Wang, P.; Di, L.B. Plasma Synthesis of Defect-Rich Flexible Carbon Cloth Decorated with PtRu Alloyed Nanoclusters for Highly Efficient pH-Universal Electrocatalytic Hydrogen Evolution. *Nanoscale* **2022**, *14*, 15942–15949. [CrossRef]
7. Wang, Y.H.; Yun, S.N.; Shi, J.; Zhang, Y.W.; Dang, J.E.; Dang, C.W.; Liu, Z.L.; Deng, Y.Y.; Yang, T.X. Defect Engineering Tuning Electron Structure of Biphasic Tungsten-Based Chalcogenide Heterostructure Improves Its Catalytic Activity for Hydrogen Evolution and Triiodide Reduction. *J. Colloid Interface Sci.* **2022**, *625*, 800–816. [CrossRef]
8. Da, P.F.; Zheng, Y.; Hu, Y.; Wu, Z.L.; Zhao, H.Y.; Wei, Y.C.; Guo, L.C.; Wang, J.J.; Wei, Y.P.; Xi, S.B.; et al. Synthesis of Bandgap-Tunable Transition Metal Sulfides through Gas-Phase Cation Exchange-Induced Topological Transformation. *Angew. Chem. Int. Ed.* **2023**, *62*, e202301802. [CrossRef]
9. Chen, X.Y.; Han, Z.; Zhang, B.; Sun, B.J.; Wang, Y.; Du, Y.C.; Han, X.J.; Xu, P. Construction of Plasmonic 1T-WS_2/2H-WS_2/CdS Heterostructures for Enhanced Solar-Driven Hydrogen Evolution. *J. Mater. Chem. A* **2022**, *10*, 24030–24040. [CrossRef]
10. Chen, S.-F.; Wu, T.-S.; Soo, Y.-L. Highly Defective Graphene Quantum Dots-Doped 1T/2H-MoS_2 as an Efficient Composite Catalyst for the Hydrogen Evolution Reaction. *Sci. Rep.* **2023**, *13*, 15184. [CrossRef]
11. Eftekhari, A. Electrocatalytic hydrogen evolution reaction: A comprehensive review. *Int. J. Hydrogen Energy* **2017**, *42*, 11053–11077. [CrossRef]
12. Dai, X.P.; Du, K.L.; Li, Z.Z.; Liu, M.Z.; Ma, Y.D.; Sun, H.; Zhang, X.; Yang, Y. Co-Doped MoS_2 Nanosheets with the Dominant CoMoS Phase Coated on Carbon as an Excellent Electrocatalyst for Hydrogen Evolution. *ACS Appl. Mater. Interfaces* **2015**, *7*, 27242–27253. [CrossRef] [PubMed]
13. Lu, Z.; Li, S.; Ning, L.; Tang, K.; Guo, Y.; You, L.; Chen, C.; Wang, G. Nickel–Iron-Layered Double Hydroxide Electrocatalyst with Nanosheets Array for High Performance of Water Splitting. *Molecules* **2024**, *29*, 2092. [CrossRef]
14. Feng, Q.L.; Mao, N.N.; Wu, J.X.; Xu, H.; Wang, C.M.; Zhang, J.; Xie, L.M. Growth of $MoS_{2(1-x)}$ Se_{2x} (x = 0.41–1.00) Monolayer Alloys with Controlled Morphology by Physical Vapor Deposition. *ACS Nano* **2015**, *9*, 7450–7455. [CrossRef]
15. Chhowalla, M.; Shin, H.S.; Eda, G.; Li, L.J.; Loh, K.P.; Zhang, H. The Chemistry of Two-Dimensional Layered Transition Metal Dichalcogenide Nanosheets. *Nat. Chem.* **2013**, *5*, 263–275. [CrossRef]
16. Shen, D.Y.; Zhao, B.; Zhang, Z.C.; Zhang, H.M.; Yang, X.D.; Huang, Z.W.; Li, B.L.; Song, R.; Jin, Y.J.; Wu, R.X.; et al. Synthesis of Group VIII Magnetic Transition Metal-Doped Monolayer $MoSe_2$. *ACS Nano* **2022**, *16*, 10623–10631. [CrossRef]
17. Zimron, O.; Zilberman, T.; Kadam, S.R.; Ghosh, S.; Kolatker, S.-L.; Neyman, A.; Bar-Ziv, R.; Bar-Sadan, M. Co-Doped $MoSe_2$ Nanoflowers as Efficient Catalysts for Electrochemical Hydrogen Evolution Reaction (HER) in Acidic and Alkaline Media. *Isr. J. Chem.* **2020**, *60*, 624–629. [CrossRef]
18. Yang, Y.Q.; Zhao, X.; Mao, H.; Ning, R.; Zheng, X.H.; Sui, J.H.; Cai, W. Nickel-doped $MoSe_2$ nanosheets with Ni-Se bond for alkaline electrocatalytic hydrogen evolution. *J. Mater. Chem. A* **2023**, *11*, 12345–12352. [CrossRef]
19. Chen, Y.P.; Huang, Y.C.; Xiong, K.Y.; Ye, X.Y.; Liu, Q.Q.; Zhuang, J.R.; Zhang, Y.F.; Zhu, J. Cooperative 3d-Metal-Doped $MoSe_2$ Catalysts for Enhanced Electrocatalytic Hydrogen Evolution Reaction. *Mol. Catal.* **2024**, *566*, 114401. [CrossRef]
20. Liu, T.; Xu, H.; Zhou, W.; Zhang, K.; Sun, Y. Computational Design of Single-Atom Catalysts: Cobalt-Doped $MoSe_2$ as a High-Performance Electrocatalyst for Hydrogen Evolution. *ACS Catal.* **2020**, *10*, 12345–12356.
21. Xu, C.; Peng, S.J.; Tan, C.L.; Ang, H.X.; Tan, H.T.; Zhang, H.; Yan, Q.Y. Ultrathin S-Doped $MoSe_2$ Nanosheets for Efficient Hydrogen Evolution. *J. Mater. Chem. A* **2014**, *2*, 5597–5601. [CrossRef]
22. Xiong, Q.Z.; Zhang, X.; Wang, H.J.; Liu, G.Q.; Wang, G.Z.; Zhang, H.M.; Zhao, H.J. One-Step Synthesis of Cobalt-Doped MoS_2 Nanosheets as Bifunctional Electrocatalysts for Overall Water Splitting under Both Acidic and Alkaline Conditions. *Chem. Commun.* **2018**, *54*, 3859–3862. [CrossRef]

23. Sun, X.; Dai, J.; Guo, Y.Q.; Wu, C.Z.; Hu, F.T.; Zhao, J.Y.; Zeng, X.C.; Xie, Y. Semimetallic Molybdenum Disulfide Ultrathin Nanosheets as an Efficient Electrocatalyst for Hydrogen Evolution. *Nanoscale* **2014**, *6*, 8359–8367. [CrossRef]
24. Zong, H.; Yu, K.; Zhu, Z. Heterostructure nanohybrids of Ni-doped $MoSe_2$ coupled with Ti_2NT_x toward efficient overall water splitting. *Electrochim. Acta* **2020**, *353*, 136598. [CrossRef]
25. Zhao, G.Q.; Wang, X.Y.; Wang, S.L.; Rui, K.; Chen, Y.P.; Yu, H.B.; Ma, J.; Dou, S.X.; Sun, W.P. Evolution Kinetics for Alkaline Water Splitting. *Chem. Asian J.* **2019**, *14*, 301–306. [CrossRef]
26. Dymerska, A.; Kukułka, W.; Wenelska, K.; Mijowska, E. Two-Dimensional Molybdenum Diselenide Tuned by Bimetal Co/Ni Nanoparticles for Oxygen Evolution Reaction. *ACS Omega* **2020**, *5*, 28730–28737. [CrossRef]
27. Venkatesh, P.S.; Kannan, N.; Babu, M.G.; Paulraj, G.; Jeganathan, K. Transition Metal Doped MoS_2 Nanosheets for Electrocatalytic Hydrogen Evolution Reaction. *Mater. Today Proc.* **2022**, *47*, 37256–37263.
28. Najafi, L.; Bellani, S.; Oropesa-Nuñez, R.; Ansaldo, A.; Prato, M.; Del Rio Castillo, A.E.; Bonaccorso, F. Engineered $MoSe_2$-based heterostructures for efficient electrochemical hydrogen evolution reaction. *Adv. Energy Mater.* **2018**, *8*, 1703212. [CrossRef]
29. Liu, Y.D.; Ren, L.; Zhang, Z.; Qi, X.; Li, H.X.; Zhong, J.X. 3D Binder-free $MoSe_2$ Nanosheets/Carbon Cloth Electrodes for Efficient and Stable Hydrogen Evolution Prepared by Simple Electrophoresis Deposition Strategy. *Sci. Rep.* **2016**, *6*, 22516. [CrossRef]
30. McCrory, C.C.L.; Jung, S.; Peters, J.C.; Jaramillo, T.F. Benchmarking Heterogeneous Electrocatalysts for the Oxygen Evolution Reaction. *J. Am. Chem. Soc.* **2013**, *135*, 16977–16987. [CrossRef]
31. Kresse, G.; Hafner, J. Ab Initio Molecular Dynamics for Liquid Metals. *Phys. Rev. B* **1993**, *47*, 558(R). [CrossRef] [PubMed]
32. Kresse, G.; Furthmüller, J.; Hafner, J. Theory of the Crystal Structures of Selenium and Tellurium: The Effect of Generalized-Gradient Corrections to the Local-Density Approximation. *Phys. Rev. B* **1994**, *50*, 13181–13190. [CrossRef] [PubMed]
33. Kresse, G.; Furthmüller, J. Efficient Iterative Schemes for Ab Initio Total-Energy Calculations Using a Plane-Wave Basis Set. *Phys. Rev. B* **1996**, *54*, 11169–11186. [CrossRef] [PubMed]
34. Perdew, J.P.; Burke, K.; Ernzerhof, M. Generalized Gradient Approximation Made Simple. *Phys. Rev. Lett.* **1996**, *77*, 3865–3868. [CrossRef]

Disclaimer/Publisher's Note: The statements, opinions and data contained in all publications are solely those of the individual author(s) and contributor(s) and not of MDPI and/or the editor(s). MDPI and/or the editor(s) disclaim responsibility for any injury to people or property resulting from any ideas, methods, instructions or products referred to in the content.